Environ Fluid Mech
DOI 10.1007/s10652-012-9256-1

ORIGINAL ARTICLE

A σ-coordinate transport model coupled with rotational boussinesq-type equations

Dae-Hong Kim · Patrick J. Lynett

Received: 7 February 2012 / Accepted: 6 October 2012

Abstract This paper describes a σ-coordinate scalar transport model coupled with a Boussinesq-type hydrodynamic model. The Boussinesq model has the ability to calculate both three-dimensional velocity distributions and the water surface motion. To capture 'dispersion' processes in open channel flow, horizontal vorticity effects induced by a bottom shear stress are included in the Boussinesq model. Thus, a reasonable representation of vertical flow structure can be captured in shallow and wavy flow fields. To solve the coupled Boussinesq and scalar transport system, a finite-volume method, based on a Godunov-type scheme with the HLL Riemann solver, is employed. Basic advection and advection–diffusion numerical tests in a non-rectangular domain were carried out and the computed results show good agreement with analytic solutions. With quantitative comparisons of dispersion experiments in an open channel, it is verified that the proposed coupled model is appropriate for both near and far field scalar transport predictions. From numerical simulations in the surf zone, physically reasonable results showing expected vertical variation are obtained.

Keywords Transport · Near field mixing · σ-coordinates · Boussinesq equation · Finite volume method

Abbreviations

BE	Boussinesq equation
DAT	Depth averaged transport equation
DIES	Depth integrated Eddy simulation
DIT	Depth integrated transport equation
NS	Navier Stokes equation
SWE	Shallow water equation

D.-H. Kim (✉)
Department of Civil Engineering, University of Seoul, Seoul, Republic of Korea
e-mail: dhkimhyd@uos.ac.kr

P. J. Lynett
Sonny Astani Department of Civil and Environmental Engineering,
University of Southern California, Los Angeles, CA, USA

Published online: 27 October 2012

List of symbols

$\mathbf{A}$	Cell side vector
c_f	Roughness coefficient
C	Scalar concentration
C_B	A model constant of BSM
$D_x,\ D_y,\ D_z$	Diffusion coefficients in the x^*, y^* : z^* directions
F_i	Dispersive stresses
$\boldsymbol{F}$	Flux vector evaluated at the cell interface
g	Gravitational acceleration
h	Water depth
H	Total water depth
$i+1/2,\ i-1/2$	Cell interfaces
k_s	Roughness height
$L,\ R$	Left and right sides of a cell interface
n	Index for the time marching
Re	Reynolds number
R_i	Breaking dissipation term
S_{ij}	Strain rate tensor
$S_L,\ S_R$	Wave speeds
$t,\ t^*$	Time
$\boldsymbol{U}$	(u, v, ω_σ)
(u, v)	Horizontal velocities
$\widetilde{u},\ \widetilde{v}$	Depth averaged horizontal velocities
$U_{\alpha i} = (U_\alpha, V_\alpha)$	Horizontal velocity at arbitrary level $z^* = z_\alpha$
u_τ	Friction velocity
$\mathcal{V}$	Volume of a computational cell
w	Vertical velocity in the physical domain
$x,\ y$	Horizontal axes in σ-coordinates
(x^*, y^*)	Horizontal axes in physical space
z^*	Vertical axis in physical space
Δt	Time step
$\Delta x,\ \Delta y$	Grid size in horizontal direction
$\Delta\sigma$	Grid size in σ direction
ζ	Free surface elevation
κ	Von Karmann constant
ν	Kinematic viscosity of water
ν_b	Wave breaking viscosity
ν_t^h	Horizontal eddy viscosity
ν_t^v	Vertical eddy viscosity
ρ	Water density
σ	Vertical axis in σ-coordinates
Γ_t	Turbulent Schmidt number
τ_i^b	Bottom shear stresses

1 Introduction

Elucidating the mixing mechanism and its prediction has long been an important and interesting topic to hydrodynamic and environmental researchers. After Taylor [24] made significant

analytical progress on the subject, various extensions were proposed by many, such as Fischer et al. [8]. In the field, however, due to many factors such as turbulence, complex geometry and boundary conditions, it is very difficult to accurately predict the scalar transport with analytical methods. Field measurement is difficult as well, as it is time intensive and often too expensive or impractical to get the many site-specific variables. Hence, using numerical methods for the investigation or prediction of mixing process can be a complementary and practical approach.

For the prediction of flow and transport in a large domain under nondispersive and hydrostatic pressure conditions, use of a coupled model composed of shallow water equation (SWE) and a depth-averaged transport equation (DAT) is one of the more common approaches. By ignoring the vertical velocity and the vertical variation of horizontal velocity, such a model can predict very efficiently flow and transport with acceptable accuracy. Additionally, SWE and DAT have consistency in view of their eigen structure; the scalar transport advection equation has the same approximate Riemann solver as the equation of tangential velocity of the homogeneous SWE [27]. The same numerical method can be applied to solve both the advection acceleration terms of SWE and the advection term of DAT [27]. However, it is not possible to get any vertical structure of flow and transport. Thus, they are limited in the prediction of near field transport [12].

For prediction of near field transport, the most physical and accurate approach among numerical methods is to solve the three-dimensional (3D) Navier–Stokes equations (NS) coupled with a 3D transport model. A 3D NS model requires massive computational resources, and it is presently not practical to apply for large domains such as rivers and coasts. Furthermore, in Cartesian coordinates, an additional difficulty arises; the irregular free surface crosses the regular computational grid constantly, and it becomes complicated to apply the pressure boundary condition precisely on the free surface [16].

As an alternative, the σ-coordinate system, which maps a nonuniform vertical domain into a rectangular domain [20], can be employed. With this approach the boundary condition on the free surface can be precisely applied if the water surface curvature is not sharp. Many successful results using σ-coordinates model, such as POM [2], ROMS [1], and GETM [5], have been reported. With the σ-coordinate method, Stansby [22] developed a 3D semi-implicit finite volume method (FVM) for the prediction of shallow water flow and transport while employing the hydrostatic pressure assumption. Stansby and Zhou [23] later incorporated a nonhydrostatic pressure solver into the numerical model mentioned above. Although they obtained closer agreement with experimental data than the hydrostatic pressure model, the nonhydrostatic pressure solver demonstrated to be a computationally expensive modification. To accommodate this cost, a hybrid approach was proposed; inclusion of nonhydrostatic pressure might need to be restricted to the parts of the flow where its influence was significant. Lin and Li (2002) developed a 3D numerical model based on the NS in a σ-coordinate system. They tested the free surface capturing capability of the proposed model, and very good results were found. To obtain accurate results, however, a requirement on the vertical resolution should be satisfied, leading to higher computational times associated with a finer mesh. To increase the computational efficiency, Yuan and Wu (2004) developed an implicit σ-coordinate finite difference model. Their modeling results were compared with several analytical solutions and laboratory experiments, and good agreement was obtained. For practical application in a river or an estuary, Lee et al. [15] developed a width-averaged 2D σ-coordinate flow model and coupled it with a transport model. Their application successfully reproduced measured data in an estuary. Bradford [3] proposed a Godunov based nonhydrostatic flow model and applied it to various wave propagation and runup problems, and later [4] to wave breaking problems in the surf zone.

A (generally) less computationally restrictive modeling approach for large-scale problems is use of the Boussinesq-type equations (BE). The BE model can calculate efficiently the vertical structure of flows in the shallow water while considering nonhydrostatic pressure, frequency dispersion of free surface gravity waves, and horizontal and vertical rotationality (e.g. [13]). Recently, Kim and Lynett [12] proposed a depth integrated eddy simulation (DIES) model, which incorporated subgrid turbulent fluctuation effects into the BE proposed by [13]. Similar to the coupling of SWE and DAT, a depth-integrated transport (DIT) model [12] can be coupled with a BE model or DIES, maintaining a consistency of physical assumptions as well as and numerical schemes. It was found that DIES and DIT could predict very well the turbulent transport in the far field. However, an inherent limitation for near field mixing exists with DIT due to a required assumption of weakly unsteady flow and vertically well-mixed conditions.

Following this previous work, the development of a coupled model using BE (or DIES) with a σ-coordinate transport model for the prediction of near and far field transport is suggested; BE is efficient and it can provide an accurate velocity field to a σ-coordinate transport model under a wide range of hydrodynamic configurations. Unlike DIT or DAT, a σ-coordinate transport model can use vertical velocity information for the prediction of vertical mixing. In addition, the pair of BE with a σ-coordinate transport model does not require a large computational cost as there is no requirement for a nonhydrostatic pressure solver.

The outline of this paper is as follows: In the next section, the advection–diffusion equation in the σ-coordinate is derived. The numerical method for the σ-coordinate transport model is then provided. Next, a brief explanation about the DIES and the coupling scheme are described. Finally, verification of the coupled model for near field and far field mixing is presented.

2 Advection–diffusion equation in σ-coordinates

2.1 Advection–diffusion equation in σ-coordinates

In a physical domain (t^*, x^*, y^*, z^*), the advection–diffusion equation is given by

$$\frac{\partial C}{\partial t^*} + u\frac{\partial C}{\partial x^*} + v\frac{\partial C}{\partial y^*} + w\frac{\partial C}{\partial z^*} = \frac{\partial}{\partial x^*}\left(D_x\frac{\partial C}{\partial x^*}\right) + \frac{\partial}{\partial y^*}\left(D_y\frac{\partial C}{\partial y^*}\right) + \frac{\partial}{\partial z^*}\left(D_z\frac{\partial C}{\partial z^*}\right) \tag{1}$$

where (x^*, y^*) represents the horizontal axes and z^* represents the vertical axis. t^* is the time and C is the concentration. (u, v) are the horizontal velocities, and w is the vertical velocity in the physical domain. D_x, D_y, and D_z are the diffusion coefficients in the x^*, y^* and z^* directions, respectively.

In this paper, the σ-coordinate space (t, x, y, σ) is defined as follows.

$$t = t^*, \quad x = x^*, \quad y = y^*, \quad \sigma = \frac{z^* + h}{H} \tag{2}$$

in which $H = h + \zeta$ is the total water depth, ζ is the free surface elevation, and h is the water depth. Using Eq. (2) the physical domain is transformed to the rectangular shaped σ-coordinates domain as shown in Fig. 1. Derivatives are transferred following the chain rule

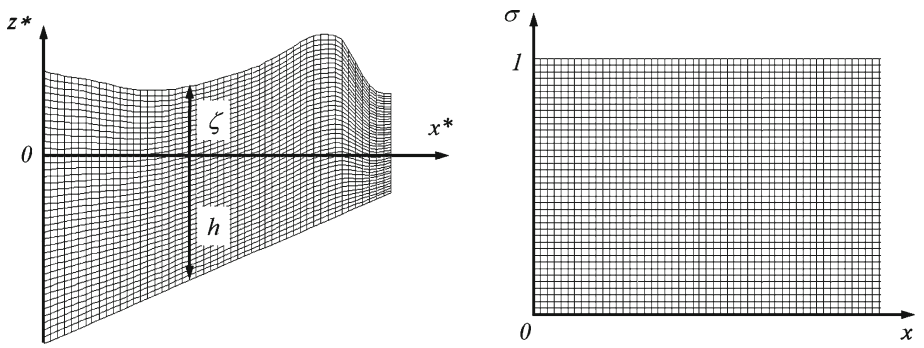

Fig. 1 Grid systems in physical domain (*left*) and σ-coordinate system (*right*)

$$\begin{aligned}
\frac{\partial f}{\partial t^*} &= \frac{\partial f}{\partial t} + \frac{\partial f}{\partial \sigma}\frac{\partial \sigma}{\partial t^*} \\
\frac{\partial f}{\partial x^*} &= \frac{\partial f}{\partial x} + \frac{\partial f}{\partial \sigma}\frac{\partial \sigma}{\partial x^*} \\
\frac{\partial f}{\partial y^*} &= \frac{\partial f}{\partial y} + \frac{\partial f}{\partial \sigma}\frac{\partial \sigma}{\partial y^*} \\
\frac{\partial f}{\partial z^*} &= \frac{\partial f}{\partial \sigma}\frac{\partial \sigma}{\partial z^*}
\end{aligned} \tag{3}$$

where $f = f(t^*, x^*, y^*, z^*)$ is some function in the physical domain. The differentiation terms on the right hand side of Eq. (3) are expressed as

$$\begin{aligned}
\frac{\partial \sigma}{\partial t^*} &= -\frac{\sigma}{H}\frac{\partial H}{\partial t} \\
\frac{\partial \sigma}{\partial x^*} &= \frac{1}{H}\frac{\partial h}{\partial x} - \frac{\sigma}{H}\frac{\partial H}{\partial x} \\
\frac{\partial \sigma}{\partial y^*} &= \frac{1}{H}\frac{\partial h}{\partial y} - \frac{\sigma}{H}\frac{\partial H}{\partial y} \\
\frac{\partial \sigma}{\partial z^*} &= \frac{1}{H}
\end{aligned} \tag{4}$$

Substituting Eqs. (3) and (4), the left hand side of Eq. (1) is transformed to

$$\frac{\partial C}{\partial t} + u\frac{\partial C}{\partial x} + v\frac{\partial C}{\partial y} + w_\sigma \frac{\partial C}{\partial \sigma} \tag{5}$$

where w_σ is given by

$$w_\sigma = -\frac{\sigma}{H}\frac{\partial H}{\partial t} + \frac{u}{H}\frac{\partial h}{\partial x} - u\frac{\sigma}{H}\frac{\partial H}{\partial x} + \frac{v}{H}\frac{\partial h}{\partial y} - v\frac{\sigma}{H}\frac{\partial H}{\partial y} + \frac{w}{H} \tag{6}$$

Similarly, by applying the chain rule to the diffusion terms, the diffusion terms in σ-coordinates can be expressed as

$$\begin{aligned}\frac{\partial}{\partial x^*}\left(D_x\frac{\partial C}{\partial x^*}\right) &= \frac{\partial}{\partial x}\left(D_x\frac{\partial C}{\partial x}\right)\\ &\quad+\frac{\partial}{\partial x}\left\{\frac{D_x}{H}\left(\frac{\partial h}{\partial x}-\sigma\frac{\partial H}{\partial x}\right)\frac{\partial C}{\partial \sigma}\right\}\\ &\quad+\frac{1}{H}\left(\frac{\partial h}{\partial x}-\sigma\frac{\partial H}{\partial x}\right)\frac{\partial}{\partial \sigma}\left(D_x\frac{\partial C}{\partial x}\right)\\ &\quad+\frac{1}{H}\left(\frac{\partial h}{\partial x}-\sigma\frac{\partial H}{\partial x}\right)\frac{\partial}{\partial \sigma}\left\{\frac{D_x}{H}\left(\frac{\partial h}{\partial x}-\sigma\frac{\partial H}{\partial x}\right)\frac{\partial C}{\partial \sigma}\right\} \qquad (7)\\ \frac{\partial}{\partial y^*}\left(D_y\frac{\partial C}{\partial y^*}\right) &= \frac{\partial}{\partial y}\left(D_y\frac{\partial C}{\partial y}\right)\\ &\quad+\frac{\partial}{\partial y}\left\{\frac{D_y}{H}\left(\frac{\partial h}{\partial y}-\sigma\frac{\partial H}{\partial y}\right)\frac{\partial C}{\partial \sigma}\right\}\\ &\quad+\frac{1}{H}\left(\frac{\partial h}{\partial y}-\sigma\frac{\partial H}{\partial y}\right)\frac{\partial}{\partial \sigma}\left(D_y\frac{\partial C}{\partial y}\right)\\ &\quad+\frac{1}{H}\left(\frac{\partial h}{\partial y}-\sigma\frac{\partial H}{\partial y}\right)\frac{\partial}{\partial \sigma}\left\{\frac{D_y}{H}\left(\frac{\partial h}{\partial y}-\sigma\frac{\partial H}{\partial y}\right)\frac{\partial C}{\partial \sigma}\right\} \qquad (8)\\ \frac{\partial}{\partial z^*}\left(D_z\frac{\partial C}{\partial z^*}\right) &= \frac{1}{H^2}\frac{\partial}{\partial \sigma}\left(D_z\frac{\partial C}{\partial \sigma}\right) \qquad (9)\end{aligned}$$

With substitution of the continuity equation and multiplication of the transformed advection and diffusion terms by H, a conservative form can be obtained:

$$\begin{aligned}&\frac{\partial HC}{\partial t}+\frac{\partial uHC}{\partial x}+\frac{\partial vHC}{\partial y}+\frac{\partial w_\sigma HC}{\partial \sigma}\\ &\quad= H\frac{\partial}{\partial x}\left(D_x\frac{\partial C}{\partial x}\right)+H\frac{\partial}{\partial x}\left\{\frac{D_x}{H}\left(\frac{\partial h}{\partial x}-\sigma\frac{\partial H}{\partial x}\right)\frac{\partial C}{\partial \sigma}\right\}\\ &\qquad+\left(\frac{\partial h}{\partial x}-\sigma\frac{\partial H}{\partial x}\right)\frac{\partial}{\partial \sigma}\left(D_x\frac{\partial C}{\partial x}\right)\\ &\qquad+\left(\frac{\partial h}{\partial x}-\sigma\frac{\partial H}{\partial x}\right)\frac{\partial}{\partial \sigma}\left\{\frac{D_x}{H}\left(\frac{\partial h}{\partial x}-\sigma\frac{\partial H}{\partial x}\right)\frac{\partial C}{\partial \sigma}\right\}\\ &\qquad+H\frac{\partial}{\partial y}\left(D_y\frac{\partial C}{\partial y}\right)+H\frac{\partial}{\partial y}\left\{\frac{D_y}{H}\left(\frac{\partial h}{\partial y}-\sigma\frac{\partial H}{\partial y}\right)\frac{\partial C}{\partial \sigma}\right\}\\ &\qquad+\left(\frac{\partial h}{\partial y}-\sigma\frac{\partial H}{\partial y}\right)\frac{\partial}{\partial \sigma}\left(D_y\frac{\partial C}{\partial y}\right)\\ &\qquad+\left(\frac{\partial h}{\partial y}-\sigma\frac{\partial H}{\partial y}\right)\frac{\partial}{\partial \sigma}\left\{\frac{D_y}{H}\left(\frac{\partial h}{\partial y}-\sigma\frac{\partial H}{\partial y}\right)\frac{\partial C}{\partial \sigma}\right\}\\ &\qquad+\frac{1}{H}\frac{\partial}{\partial \sigma}\left(D_z\frac{\partial C}{\partial \sigma}\right) \qquad (10)\end{aligned}$$

This conservative-form equation has similar numerical properties to the DIES with which it will be coupled.

2.2 Boundary conditions

By applying the chain rule to the boundary conditions, the following boundary conditions are obtained. The Dirichlet boundary condition remains the same, but the Neumann boundary condition is changed. At the bottom and at the water surface, the conditions are

$$\frac{\partial C}{\partial z^*} = \frac{1}{H}\frac{\partial C}{\partial \sigma} = 0 \tag{11}$$

Along a vertical side wall, the boundary condition is

$$\frac{\partial C}{\partial x^*} = \frac{\partial C}{\partial x} + \left(\frac{1}{H}\frac{\partial h}{\partial x} - \frac{\sigma}{H}\frac{\partial H}{\partial x}\right)\frac{\partial C}{\partial \sigma} = 0 \tag{12}$$

3 Numerical methods for σ-coordinates transport model

3.1 Fourth-order accurate FVM for advection terms

By integrating the advection equation over a cell, the equation becomes

$$\frac{\partial HC}{\partial t} + \frac{1}{\mathcal{V}}\sum \boldsymbol{F}\cdot\mathbf{A} = 0 \tag{13}$$

where $\mathcal{V}$ is the volume of a computational cell, $\boldsymbol{F}$ is a flux vector evaluated at the cell interface, which is defined as $\boldsymbol{F} = CH\boldsymbol{U}$, $\boldsymbol{U} = (u, v, \omega_\sigma)$, and $\mathbf{A}$ is the cell side vector defined as the cell side area multiplied by the outward unit normal vector. In order to keep computational consistency with the DIES model, the value of C at the interface was evaluated by using the fourth-order compact MUSCL TVD scheme [29] as follows:

$$C^L_{i+1/2} = C_i + \frac{1}{6}\left\{\Delta^*\overline{C}_{i-1/2} + 2\Delta^*\widetilde{C}_{i+1/2}\right\} \tag{14}$$

$$C^R_{i+1/2} = C_{i+1} - \frac{1}{6}\left\{2\Delta^*\overline{C}_{i+1/2} + 2\Delta^*\widetilde{C}_{i+3/2}\right\} \tag{15}$$

where the subscripts $i+1/2$ and $i-1/2$ refer to the interface locations and L and R refer to the left and the right sides of a cell interface, respectively. The other terms are given by

$$\Delta^*\overline{C}_{i-1/2} = minmod\left(\Delta^*C_{i-1/2}, b\Delta^*C_{i+1/2}\right) \tag{16}$$

$$\Delta^*\widetilde{C}_{i+1/2} = minmod\left(\Delta^*C_{i+1/2}, b\Delta^*C_{i-1/2}\right) \tag{17}$$

$$\Delta^*\overline{C}_{i+1/2} = minmod\left(\Delta^*C_{i+1/2}, b\Delta^*C_{i+3/2}\right) \tag{18}$$

$$\Delta^*\widetilde{C}_{i+3/2} = minmod\left(\Delta^*C_{i+3/2}, b\Delta^*C_{i+1/2}\right) \tag{19}$$

$$\Delta^*C_{i+1/2} = \Delta C_{i+1/2} - \frac{1}{6}\Delta^3\overline{C}_{i+1/2} \tag{20}$$

$$\Delta^3\overline{C}_{i+1/2} = \Delta\overline{C}_{i-1/2} - 2\Delta\overline{C}_{i+1/2} + \Delta\overline{C}_{i+3/2} \tag{21}$$

$$\Delta\overline{C}_{i-1/2} = minmod\left(\Delta C_{i-1/2}, b_1\Delta C_{i+1/2}, b_1\Delta C_{i+3/2}\right) \tag{22}$$

$$\Delta\overline{C}_{i+1/2} = minmod\left(\Delta C_{i+1/2}, b_1\Delta C_{i+3/2}, b_1\Delta C_{i-1/2}\right) \tag{23}$$

$$\Delta\overline{C}_{i+3/2} = minmod\left(\Delta C_{i+3/2}, b_1\Delta C_{i-1/2}, b_1\Delta C_{i+1/2}\right) \tag{24}$$

$$minmod(i, j) = sign(i)\max\left[0, \min\left\{|i|, sign(i)\right\}\right] \tag{25}$$

$$minmod(i, j, k) = sign(i)\max\left[0, \min\left\{|i|, sign(i), sign(i)k\right\}\right] \tag{26}$$

in which the coefficients $b_1 = 2$ and $1 < b \leq 4$. Further details of this numerical scheme are described in [29].

After constructing the interface values, the numerical fluxes were computed by the HLL approximate Riemann solver [26]:

$$\boldsymbol{F}_{i+1/2} = \begin{cases} \boldsymbol{F}_L, \ 0 \leq S_L \\ \boldsymbol{F}_*, \ S_L \leq 0 \leq S_R \\ \boldsymbol{F}_R, \ 0 \geq S_R \end{cases} \tag{27}$$

where

$$\boldsymbol{F}_* = \frac{S_R \boldsymbol{F}_L - S_L \boldsymbol{F}_R + S_R S_L \left(\boldsymbol{U}_R - \boldsymbol{U}_L\right)}{S_R - S_L} \tag{28}$$

and S_L and S_R are the wave speeds. Further details of the HLL approximate Riemann solver are clearly explained in [26].

3.2 Fourth-order accurate FVM for diffusion terms

A cell averaged value $\overline{C}_i$ is defined as

$$\overline{C}_i = \frac{1}{\Delta x} \int_{x_{i-1/2}}^{x_{i+1/2}} C(x) dx \tag{29}$$

and by substituting the cell averaged value into the Taylor series $C = C_{1+1/2} + xC'_{1+1/2} + x^2/2C''_{1+1/2} + x^3/6C'''_{1+1/2} + x^4/24C''''_{1+1/2} + \cdots$, the cell average can be expressed with values defined at cell interfaces [13]. For example, $\overline{C}_i$ is given by

$$\overline{C}_i = C_{i+1/2} - \frac{\Delta x}{2} C'_{i+1/2} + \frac{\Delta x^2}{6} C''_{i+1/2} - \frac{\Delta x^3}{24} C'''_{1+1/2} + \cdots \tag{30}$$

where the subscript i refers to the index of a cell and Δx is the grid size. From the combination of several Taylor series expansions, fourth-order accurate discretization equations for the FVM can be obtained:

$$C_{i+1/2} = \frac{7\left(\overline{C}_{i+1} + \overline{C}_i\right) - \left(\overline{C}_{i+2} + \overline{C}_{i-1}\right)}{12} + O\left(\Delta x^4\right) \tag{31}$$

$$C'_{i+1/2} = \frac{15\left(\overline{C}_{i+1} - \overline{C}_i\right) - \left(\overline{C}_{i+2} - \overline{C}_{i-1}\right)}{12\Delta x} + O\left(\Delta x^4\right) \tag{32}$$

3.3 Time integration

The third-order Adams–Bashforth predictor and the fourth-order Adams–Moulton corrector scheme were used for the time integration. In the predictor step,

$$HC^{n+1} = HC^n + \frac{\Delta t}{12}\left(23A^n - 16A^{n-1} + 5A^{n-2}\right) \tag{33}$$

and in the corrector step,

$$HC^{n+1} = HC^n + \frac{\Delta t}{24}\left(9A^{n+1} + 19A^n - 5A^{n-1} + A^{n-2}\right) \tag{34}$$

where n is the index for the time marching and Δt is the time step. A is given in the Appendix. During the corrector step, the convergence error defined as $\sum |C^{n+1} - C_*^{n+1}| / \sum |C^{n+1}|$ was required to be less than 10^{-4} for all the computations given in this paper.

4 Depth-integrated Eddy simulation model

4.1 DIES model

As mentioned above, for the numerical computation of shallow and wavy flows in a large domain, use of the BE has become common. Typically, however, assuming potential flow in the derivation can result in the BE yielding an inaccurate vertical velocity structure when viscous effects are important [17], which can then result in poor prediction of near field mixing. For example, with uniform flow in a prismatic channel, the BE based on a potential flow assumption should predict a vertically uniform velocity field, which is not physically sensible in the presence of any bottom stress.

By including 3D vorticity effects in the fully nonlinear BE, Kim et al. [13] showed that a BE could reasonably model vertical flow structure in a weakly dispersive (here, frequency dispersion) flow environment. In addition, Kim and Lynett[12] proposed a DIES model which incorporated a stochastic backscatter model (BSM) [10] into the BE framework of Kim et al. [13]. With the BSM, the DIES can simulate the subgrid-scale turbulent fluctuation effects on turbulent mixing and scalar transport by long waves and currents. Hence, in this paper, the DIES system is used as the governing equations for flow:

$$\frac{\partial \zeta}{\partial t^*} + \frac{\partial H U_{\alpha i}}{\partial x_i^*} + \alpha + \alpha^v = 0 \tag{35}$$

$$\begin{aligned} \frac{\partial H U_{\alpha i}}{\partial t^*} &+ \frac{\partial H U_{\alpha i} U_{\alpha j}}{\partial x_j^*} + gH \frac{\partial \zeta}{\partial x_i^*} \\ &+ H\left(\beta_i + \gamma_i + \beta_i^v + \gamma_i^v\right) + U_{\alpha i}\left(\alpha + \alpha^v\right) \\ &- H \frac{\partial}{\partial x_j^*}\left(2\nu_t^h S_{ij}\right) + 2H\nu_t^v \frac{\partial}{\partial x_i^*}\left(\frac{\partial U_{\alpha j}}{\partial x_j^*}\right) \\ &+ \frac{\tau_i^b}{\rho} - HR_i - HF_i = 0 \end{aligned} \tag{36}$$

where the subscripts $i, j = (1, 2)$ and $U_{\alpha i} = (U_\alpha, V_\alpha)$ is the horizontal velocity at arbitrary level $z^* = z_\alpha$. g is the gravitational acceleration, ρ is the water density, and S_{ij} is a strain rate tensor. ν_t^h is the horizontal eddy viscosity and is modeled using the Smagorinsky model [21] with $C_s = 0.2$ as follows:

$$\nu_t^h = C_s^2 \Delta x \Delta y \left[2\left(\frac{\partial U_\alpha}{\partial x^*}\right)^2 + 2\left(\frac{\partial V_\alpha}{\partial y^*}\right)^2 + 2S^2 + \left(\frac{\partial V_\alpha}{\partial x^*} + \frac{\partial U_\alpha}{\partial y^*}\right)^2 \right]^{1/2} \tag{37}$$

in which $S = (\partial U_\alpha / \partial x^* + \partial V_\alpha / \partial y^*)$. The vertical eddy viscosity is modeled by $\nu_t^v = C_h H u_\tau$ where $C_h = \kappa/6$ is used following [7] with the von Karman constant $\kappa = 0.4$ and u_τ is the friction velocity. The bottom shear stress was modeled by a quadratic friction equation:

$$\tau_x^b = c_f \rho \widetilde{u} \sqrt{\widetilde{u}^2 + \widetilde{v}^2}, \quad \tau_y^b = c_f \rho \widetilde{v} \sqrt{\widetilde{u}^2 + \widetilde{v}^2} \tag{38}$$

where $(\tau_x^b, \tau_y^b) = \tau_i^b$ are the bottom shear stresses in the x and y directions, respectively. The roughness coefficient is given by $c_f = f/4$ [6] and f should be estimated using the Moody diagram. In this paper, f was calculated by the formula proposed by Haaland [9], which is an explicit approximation of the Moody diagram. $\widetilde{u}$ and $\widetilde{v}$ refer to the depth-averaged velocities. R_i is the breaking related dissipation term [11]. The F_i term represents dispersive stresses approximated with the BSM proposed by Hinterberger et al. [10]:

$$F_i = C_B \frac{\sqrt{\widetilde{u}^2 + \widetilde{v}^2}}{H} \sqrt{\frac{\nu \sqrt{c_f}}{\Delta t}} r_i \tag{39}$$

where ν is the kinematic viscosity of water, C_B is a model constant and r_i is a random number which has a mean of zero. Further details of the BSM are described in Hinterberger et al. [10]. In Eq. (35), α and β_i are higher-order terms related to frequency dispersion, and α^v, β_i^v, γ_i and γ_i^v are the vorticity related higher-order terms. Full expression of these terms is given in Appendix.

4.2 Numerical methods for flow model

To solve the DIES, the same numerical methods as used for the solution of the transport equation were employed. To solve the leading-order terms of the DIES, the fourth-order accurate MUSCL FVM [29] with the HLL Riemann solver [26] was used. For the higher-order terms, the same finite volume discretization equations (31) and (32) were used. The time integration used the third-order Adams–Bashforth predictor and the fourth-order Adams–Moulton corrector scheme. Details of the numerical methods for flow are described in Kim et al. [13].

4.3 Velocity profiles by the DIES model

Based on the $(\zeta, U_\alpha, V_\alpha)$ computed by the DIES, the horizontal velocity at z^* can be obtained by

$$\begin{aligned} u(z^*) = U_\alpha &+ \frac{1}{2}\left(z_\alpha^2 - z^{*2}\right) \frac{\partial}{\partial x^*}\left(\frac{\partial U_\alpha}{\partial x^*} + \frac{\partial V_\alpha}{\partial y^*}\right) \\ &+ \left(z_a - z^*\right) \frac{\partial}{\partial x^*}\left(\frac{\partial h U_\alpha}{\partial x^*} + \frac{\partial h V_\alpha}{\partial y^*}\right) \\ &+ \psi_x \left\{\frac{1}{2}\left(z_\alpha^2 - z^{*2}\right) + \zeta\left(z^* - z_\alpha\right)\right\} \end{aligned} \tag{40}$$

$$\begin{aligned} v(z^*) = V_\alpha &+ \frac{1}{2}\left(z_\alpha^2 - z^{*2}\right) \frac{\partial}{\partial y^*}\left(\frac{\partial U_\alpha}{\partial x^*} + \frac{\partial V_\alpha}{\partial y^*}\right) \\ &+ \left(z_a - z^*\right) \frac{\partial}{\partial y^*}\left(\frac{\partial h U_\alpha}{\partial x^*} + \frac{\partial h V_\alpha}{\partial y^*}\right) \\ &+ \psi_y \left\{\frac{1}{2}\left(z_\alpha^2 - z^{2*}\right) + \zeta\left(z^* - z_\alpha\right)\right\} \end{aligned} \tag{41}$$

where $\left(\psi_x, \psi_y\right) = \tau_i^b / \left(\rho \nu_t^v H\right)$ and the vertical velocity at z^* is given by

$$w(z^*) = -z^*\left(\frac{\partial u}{\partial x^*} + \frac{\partial v}{\partial y^*}\right) - \left(\frac{\partial hu}{\partial x^*} + \frac{\partial hv}{\partial y^*}\right) \tag{42}$$

The coupling procedure is very simple: Transfer the $H = (\zeta + h)$ and the (u, v, w_σ) calculated by the DIES and Eqs. (6) and (40) through (41) to the scalar transport equation in σ-coordinates, Eq. (10).

5 Numerical tests

5.1 Numerical test for transport model

In this section, the σ-coordinate transport model is tested. First, as a basic test, a simple advection problem in a two-dimensional (vertical) non-rectangular physical domain was investigated. This particular configuration was chosen due to the existence of an analytical solution [28]. The computational grid has two vertical side boundaries and a flat top boundary as shown in Fig. 2. However, the bottom boundary of the computational domain has a sinusoidal shape given by the function

$$h\left(x^*\right) = 5000 - 250 \times \sin\left(0.002x^*\right) \ (m) \tag{43}$$

Thus, the wave height of the bottom boundary is 10 % of the mean height of the computational domain and the maximum bottom slope is 0.5. In this test, an analytical velocity distribution was imposed without solving the DIES model. The flow was assumed to rotate about the center of the domain with a constant angular velocity of 0.314 rad/h, thus it rotates one circle per 20 h. This is the velocity field utilized for the analytical solution to this problem by [28]. The initial concentration is given by

$$C_o(x^*, z^*) = \exp\left\{-\frac{(x^* - x_c)^2 + (z^* - z_c)^2}{2\theta^2}\right\} \tag{44}$$

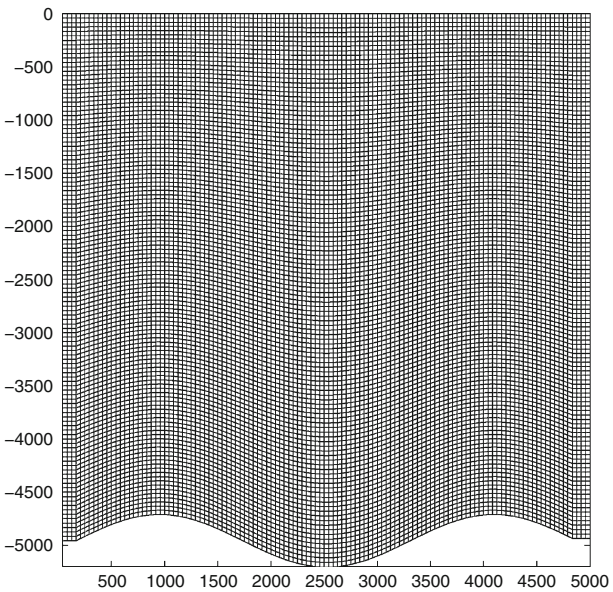

Fig. 2 Non-rectangular domain for test problem

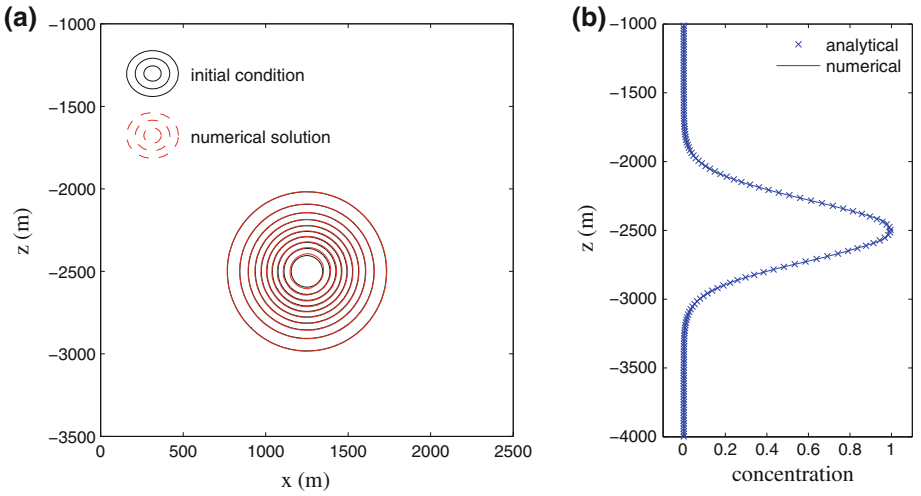

Fig. 3 Pure advection test result after one circulation. **a** Concentration contours. **b** Vertical profile at $x = 1{,}250\,\mathrm{m}$

where $x_c = 1{,}250\,\mathrm{m}$, $z_c = -2{,}500\,\mathrm{m}$ and $\theta = 220\,\mathrm{m}$. Thus, the maximum initial concentration is 1.0. The computational domain is composed of 250×250 grid points and a time step $\Delta t = 40$ second was used. Figure 3a shows the contours of the initial and the computed concentrations at $t = 20\,\mathrm{h}$. Figure 3b shows the concentration profile at $x^* = 1{,}250\,\mathrm{m}$ when $t = 20\,\mathrm{h}$, where the maximum value of the computed concentration is 0.985. As can be seen from the figures, close agreement with the analytical solution is obtained in this non-rectangular domain.

Next, an advection–diffusion problem is tested in the same flow field and with the same computational grid. For diffusion, $D_x = D_z = 0.1\,\mathrm{m}^2/\mathrm{s}$ is imposed. For the initial concentration profile equation, $\theta = 200\,\mathrm{m}$ is used. Figure 4 shows the comparisons of the computed results to the analytical solution [28] for $t = 5$, $t = 10$, $t = 15$, and $t = 20\,\mathrm{h}$. Good agreement with the analytical solutions is also obtained in the advection–diffusion test, and therefore it can be stated that the numerical solution technique utilized here is accurate for this case.

5.2 Test for velocity profile of DIES in vertical direction

To apply the coupled model in shallow and wavy flows like surf zones or rivers, it is important to have the ability to predict both the vertical and horizontal structure of the velocity field. This is tested here; note, however, that this particular test is unrelated to the transport model as only the hydrodynamics are examined. The outcome of this comparison will be used to justify numerical simulations of surf zone transport presented later.

For verification of velocity profiles in the surf zone where strong undertow exists, two comparisons are presented in this section. First, the laboratory experimental data measured by [25] are compared with the velocity profile obtained by Eq. (40). In the experiment, a wave train with a 0.089 m wave height and a 5.0 second period was generated with a depth, $h = 0.4\,\mathrm{m}$, at the wavemaker. On the opposite side, a 1/35 sloped bottom was installed. Further details of the laboratory experiments are described in the reference. Figure 5 shows good agreement between the computed water surface elevation and the experimental data.

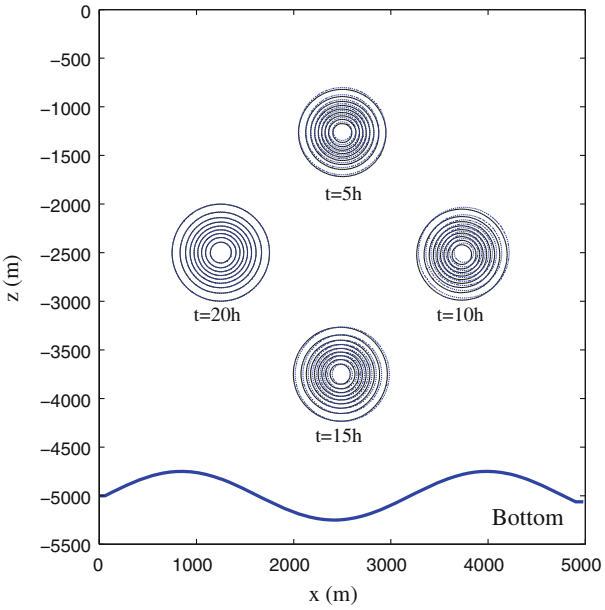

Fig. 4 Advection–diffusion test results. *Solid line* computational results, *dotted line* analytical solutions

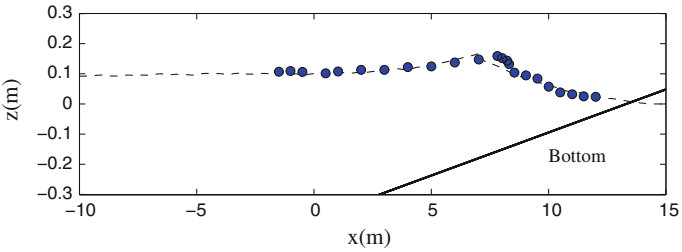

Fig. 5 Comparison of the crest level based on the phase averaged water surface elevation. *Dots* measured data (by [25]), *line* numerical results

The velocities computed by Eq. (40) are shown with the measured data in Fig. 6. Acceptable agreement with the measured data are obtained considering the simplicity of the breaking model and, in particular, the lack of any vertical structure to the numerical eddy viscosity in the surf zone.

For another comparison, the experimental data measured by Nadaoka and Kondoh [18] are used. In their experiment, the wave height was 0.219 m and the wave period was 2.34 s. The water depth was $h = 0.7$ m at the wavemaker and the slope of the beach was 1/20. Figure 7 shows the measured data and the computed results by the DIES model. Although some disagreement is apparent near the bottom where $h = 0.107$ m and $h = 0.157$ m, the computed results and the measured data are generally in reasonable agreements from the bottom to the water surface. Considering the two comparisons, it is expected that the DIES can present a reasonable vertical structure of velocity in surf zone. This will provide some confidence that wave-induced transport in the surf zone—at least that governed by the mean flow—should be reasonably captured by the model presented here.

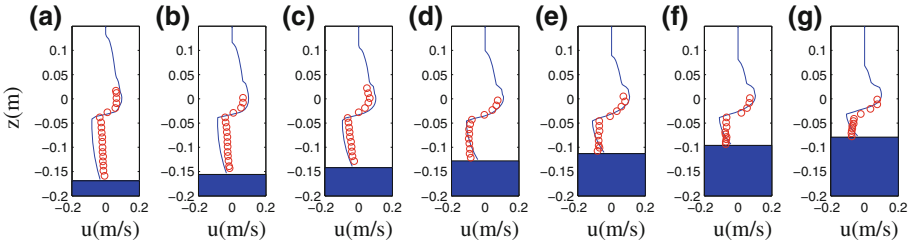

Fig. 6 Vertical profiles of phase averaged horizontal velocity at **a** $h = 0.169$ m, **b** $h = 0.156$ m, **c** $h = 0.142$ m, **d** $h = 0.128$ m, **e** $h = 0.113$ m, **f** $h = 0.096$ m, **g** $h = 0.079$ m. *Dots* experimental data (by [25]), *solid line* numerical results

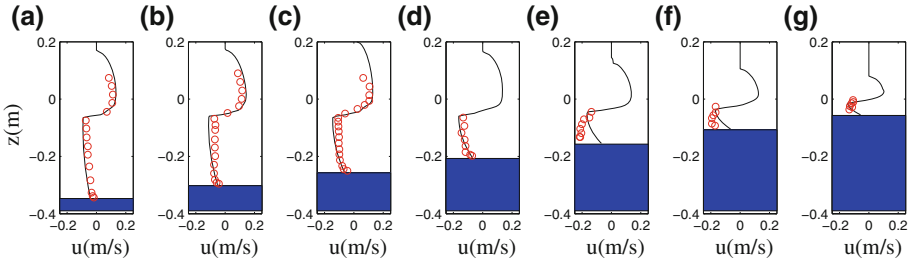

Fig. 7 Vertical profiles of phase averaged horizontal velocity at **a** $h = 0.347$ m, **b** $h = 0.302$ m, **c** $h = 0.257$ m, **d** $h = 0.207$ m, **e** $h = 0.157$ m, **f** $h = 0.107$ m, **g** $h = 0.057$ m. *Dots* experimental data (by [18]), *solid line* numerical results

6 Mixing simulations in near and far field

6.1 Dispersion simulation in open channel

In this section, we test dispersion (here, turbulent dispersion) caused by nonuniform velocity profiles and vertical diffusion. For the test, open channel flow tested by Nokes and Wood [19] is simulated using the proposed model. The cross section of the open channel is rectangular and the bottom slope is 0.00047. The water depth is 0.05 m and the streamwise direction velocity is 0.236 m/s resulting in a Reynolds number $Re = 10{,}700$. The friction factor was estimated as $f = 0.0282$ by [19]. For the numerical simulations, $\Delta x = \Delta y = 0.0125$ m are used.

Figure 8 shows the time averaged velocity profiles, and here the computed velocity profile shows reasonable agreement with the measured data. This is simply an indication that the DIES model is properly predicting the mean vertical flow structure, given the input friction factor. Figure 9 shows the computed scalar transport results when a scalar column was injected uniformly as an initial concentration. At some short distance downstream, the scalar column becomes stretched and has a curved shape when the horizontal vorticity effects are considered (Fig. 9a). Due to the curved shape and vertical turbulent diffusion, vertical diffusive flux can be amplified, which leads to the 'dispersion' process. However, when the horizontal vorticity effects are neglected, the vertical velocity profile is nearly constant and only the horizontal turbulent diffusion can be observed in this problem as shown in Fig. 9b. Thus, incorrect mixing results can be predicted in near field unless horizontal vorticity effects are considered.

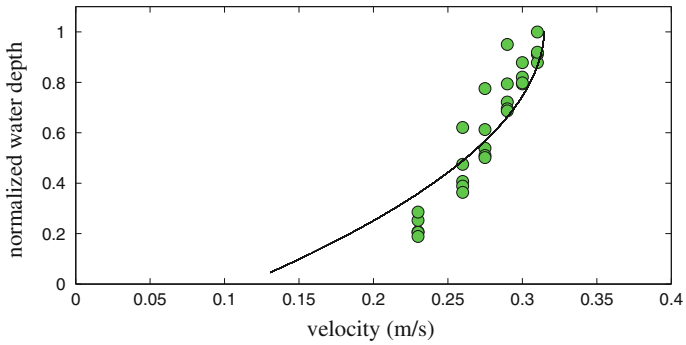

Fig. 8 Time averaged velocity distribution. *Circle* experimental data (by [19]), *line* computational result

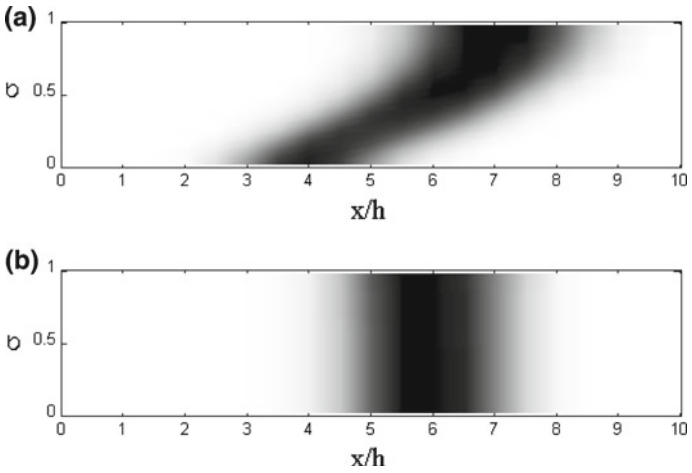

Fig. 9 Snapshot of computed scalar distributions. **a** With horizontal vorticity. **b** Without horizontal vorticity

For the purpose of quantitative verification, two laboratory experimental cases are simulated in the same flow field. The experiments were performed by [19]. With respect to the vertical direction in σ-coordinates, $\Delta\sigma = 1/21$ was used. The turbulent diffusion coefficients are evaluated as $D_x = D_y = \nu_t^h/\Gamma_t$, $D_z = \nu_t^v/\Gamma_t$ where the turbulent Schmidt number $\Gamma_t = 1.0$, and $C_B = 50$. At an upstream point of the channel, the source is released continuously.

The instantaneous computed scalar distributions are shown in Fig. 10. Figure 10a, b shows the result when the scalar was released at $\sigma = 0.24$ and $\sigma = 0.57$, respectively. Several qualitative interpretations are possible from the figures. First, the effect of the different injection levels is captured well, which is beyond of the inherent limitation of DAT or DIT. Second, we can see that parabolic structures are formed and then diffused into the vertical direction while flowing downstream; that is, the dispersion process in an open channel was modeled. Last, randomness due to the turbulence effects could be approximated by including the BSM.

For quantitative verification, time-averaged concentration data at various locations and levels are compared. As shown in Fig. 11, the measured concentration data and the computed concentration results show good agreement. On particular note is that even in the near field ($x/h <\sim 10$), the computational results closely coincide with the measured data. If we

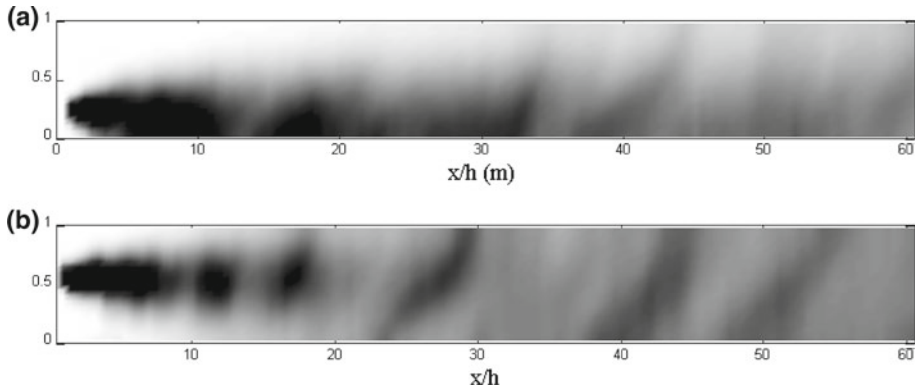

Fig. 10 Instantaneous computed concentration distribution (*black color* means higher concentration). **a** Injection level $\sigma = 0.24$. **b** Injection level $\sigma = 0.57$

had used a horizontal 2D transport model then all the relative concentration should be 1.0. Therefore, it can be concluded that the proposed σ-coordinate transport model coupled with the DIES model, which includes the horizontal vorticity, has the capability of accurately predicting both near and far field mixing in shallow flows. It needs to be mentioned that the computational results including the dispersive stress modeled by the BSM may not be regarded as convergent results at an instantaneous time. The BSM is a stochastic model, which can affect the local conservation of momentum. However, as shown in Figs. 8 and 11, the time-averaged values should converge as the random number (r_i) in the BSM has a zero mean.

6.2 Transport simulations in surf zone

In this section, the applicability of the proposed model for surf zone transport is investigated qualitatively. The computational domain depicted in Fig. 12 is composed of a beach with a constant slope of 1/35 and a horizontal plane with $h = 0.4$ m, similar to the Ting and Kirby case examined above. The wave source is located at $x = 10$ m and a sponge layer is installed at the left boundary. In the proximity of the breaking point, two contaminants are initially located at two different depths, one on the bed (Case A) and the other near the free surface (Case B). The two cases are simulated separately. A regular series of waves with an amplitude of 0.086 m, a period of 3.33 s, and a wavelength of 6.44 m are generated. For the calculations of the bottom friction terms, a roughness height of $k_s = 0.0001$ m was used and the friction factor calculated dynamically based on the instantaneous Reynolds number. The BSM is not included in this section. The entire computational domain is composed of 600×30 computational cells.

For the estimation of the diffusion coefficients, the breaking related dissipation term, R_i, was added to the turbulent eddy viscosity terms in these simulations as follows.

$$D_x = (\nu_t^h + \nu_b)/\Gamma_t \tag{45}$$

$$D_z = (\nu_t^v + \nu_b)/\Gamma_t \tag{46}$$

where ν_b is the viscosity for the calculation of the dissipation by wave breaking [11]. As in the previous section, the turbulent Schmidt number $\Gamma_t = 1.0$. An instantaneous snapshot of the water surface profile and the horizontal and the vertical velocities computed by the

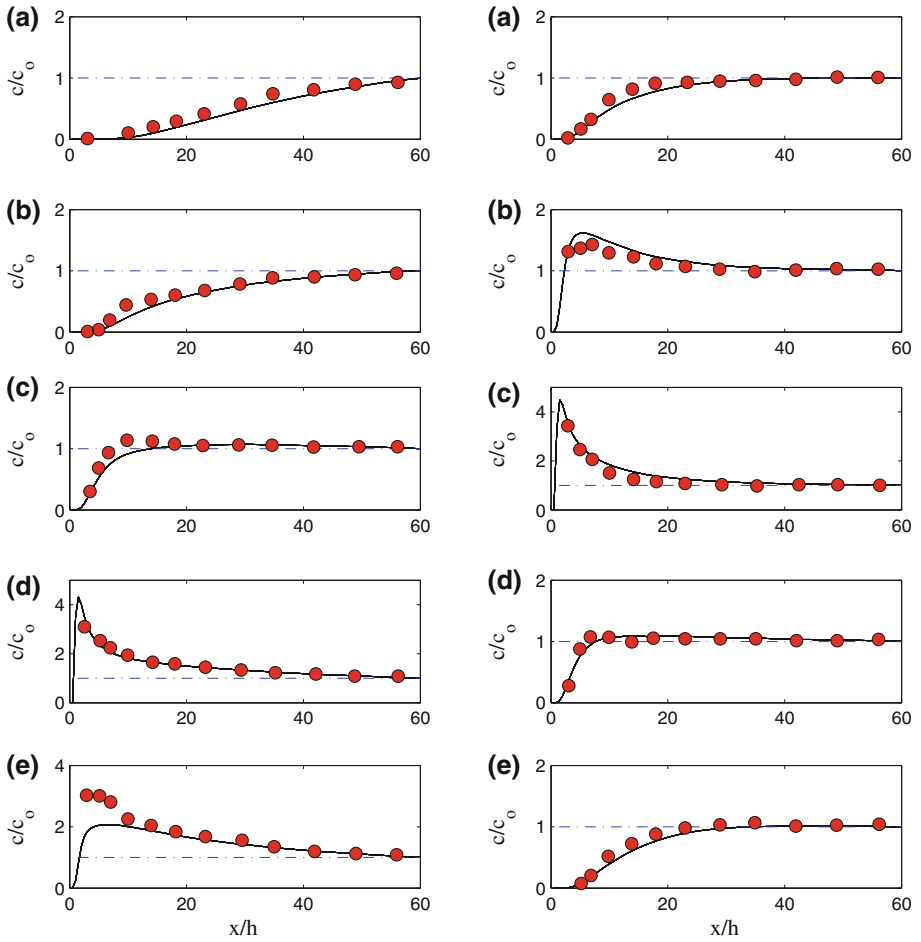

Fig. 11 Time averaged concentration distributions at various level at **a** $\sigma = 0.9$, **b** $\sigma = 0.7$, **c** $\sigma = 0.5$, **d** $\sigma = 0.3$, **e** $\sigma = 0.1$. *Circle* measured data [19], *solid line* computational results, *dotted line* depth averaged concentration. Source injection levels: *left* $\sigma = 0.24$, *right* $\sigma = 0.57$

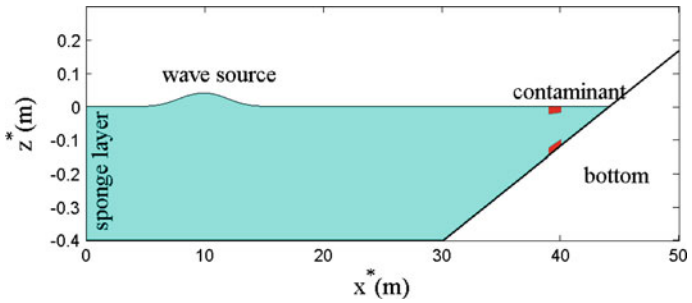

Fig. 12 Schematic of transport test in surf zone

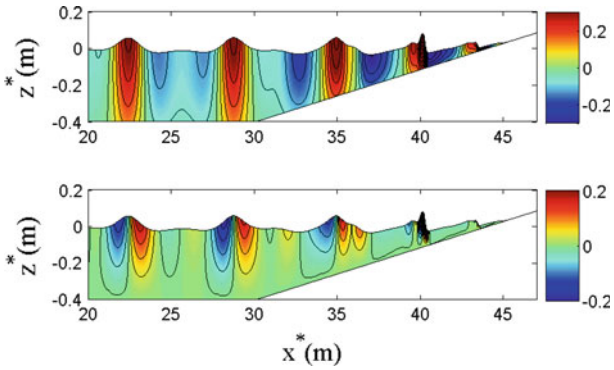

Fig. 13 Snapshot of velocity distributions by DIES model. *Upper* horizontal velocity (m/s), *lower* vertical velocity (m/s). Positive value represents shoreward direction

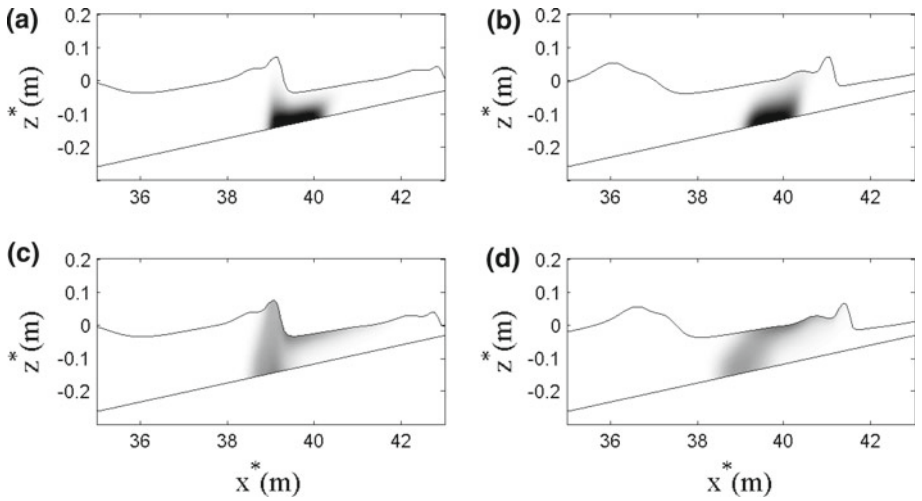

Fig. 14 Scalar concentration by the numerical simulation for case A. **a** $t = 25.4$ s, **b** $t = 27.0$ s, **c** $t = 55.4$ s, **d** $t = 57.3$ s

DIES model is given in Fig. 13. Clearly, non-uniform horizontal and vertical velocities are observed.

Figure 14 shows the computed scalar distributions for Case A (scalar initially on the bed). The scalar is partially advected from the bottom to the water surface by the vertical velocity component and then carried toward the shore by the wave crests as can be seen at Fig. 14a, b However, the scalar which was transported to the water surface by advection and diffusion did not follow the progressive wave. Soon, as can be seen from Fig. 14c, d, the clouds of the scalar become detached from the wave crests. Only a fraction of the scalar moves to the shoreline near the water surface. Near the bottom, the clouds of scalar generally move in the seaward direction. A similar phenomenon was observed in numerical simulations using a NS model with $k-\epsilon$ turbulence closure [16]. For Case B, near the surface, the clouds of the scalar are also transported to the shoreline as shown in Fig. 15a. As can be seen from Fig. 15b, after the part of scalar is transported to the bottom, the scalar cloud moves in the seaward direction. These overall movements of Case A and Case B can be regarded physically reasonable by

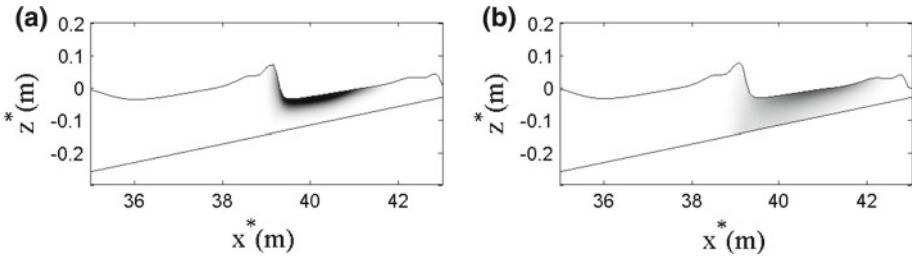

Fig. 15 Scalar concentration by the numerical simulation for case B. **a** $t = 25.4$ s, **b** $t = 55.4$ s

reviewing the phase-averaged velocity distributions of Figs. 6 and 7, where the flux under the wave crest is moving offshore (undertow) and the flux due to the wave crest shows the opposite direction, towards the shoreline.

In regard to the extent to which these results should be trusted, it should be noted that D_x and D_y are depth varying values in reality. In the surf zone, diffusion coefficients are much larger at the surface than at the bottom due to wave breaking. However, in this simulation, D_x and D_y are evaluated as vertically invariant constants as the viscosities in Eqs. (40) and (41) are based on a depth-integrated model. This physical mismatch could lead to a numerical prediction that underestimates above-trough mixing and vice-versa below-trough. To remove this limitation, the hydrodynamic model would need to be coupled with a vertically resolving turbulence model, which is not attempted here. Currently, however, this issue cannot be investigated quantitatively, as there is no existing dataset that includes both high, accurate resolution velocity profiles and scalar transport under breaking waves.

7 Summary

For the efficient prediction of near and far field mixing in shallow and wavy flows, a σ-coordinate transport model was coupled with the DIES model for weakly dispersive, turbulent and rotational flows. A basic advection test and a basic advection–diffusion test using the σ-coordinate transport model were each carried out in a nonuniform physical domain and good agreement with analytical solutions were obtained. The velocity profile estimated by the DIES model agreed reasonably well with experimental data in an open channel and a surf zone, which is a prerequisite of accurate scalar transport prediction. From comparisons with the turbulent dispersion experiments, quantitative verification of the proposed model for near field and far field mixing was recognized. From the numerical simulations in a surf zone, qualitatively reasonable results were obtained. However, there was a limitation in the evaluation of proper diffusion coefficients. Due to the use of depth-integrated hydrodynamics, the diffusion coefficients become depth-invariant. In addition, though it is not investigated intensively, the coupled model should be much more efficient than the combination using 3D NS models. Thus, numerical simulations in a large domain can be achieved with affordable computational costs by using the proposed model.

Ongoing developments of the proposed coupled model are examining how to consider the turbulence effects generated by wave breaking in surf zone. For certain wave breaking has significant impacts on vertical and horizontal transport in surf zone. If depth varying diffusion coefficients considering wave breaking can be considered, then the accuracy of the prediction will be improved greatly. In addition, proper consideration for the density can make it possible to develop more sophisticate models for sediment transport.

Appendix

$$
\begin{aligned}
A = & -\frac{\partial uHC}{\partial x} - \frac{\partial vHC}{\partial y} - \frac{\partial w_\sigma HC}{\partial \sigma} \\
& + H\frac{\partial}{\partial x}\left(D_x\frac{\partial C}{\partial x}\right) + H\frac{\partial}{\partial x}\left\{\frac{D_x}{H}\left(\frac{\partial h}{\partial x} - \sigma\frac{\partial H}{\partial x}\right)\frac{\partial C}{\partial \sigma}\right\} \\
& + \left(\frac{\partial h}{\partial x} - \sigma\frac{\partial H}{\partial x}\right)\frac{\partial}{\partial \sigma}\left(D_x\frac{\partial C}{\partial x}\right) \\
& + \left(\frac{\partial h}{\partial x} - \sigma\frac{\partial H}{\partial x}\right)\frac{\partial}{\partial \sigma}\left\{\frac{D_x}{H}\left(\frac{\partial h}{\partial x} - \sigma\frac{\partial H}{\partial x}\right)\frac{\partial C}{\partial \sigma}\right\} \\
& + H\frac{\partial}{\partial y}\left(D_y\frac{\partial C}{\partial y}\right) + H\frac{\partial}{\partial y}\left\{\frac{D_y}{H}\left(\frac{\partial h}{\partial y} - \sigma\frac{\partial H}{\partial y}\right)\frac{\partial C}{\partial \sigma}\right\} \\
& + \left(\frac{\partial h}{\partial y} - \sigma\frac{\partial H}{\partial y}\right)\frac{\partial}{\partial \sigma}\left(D_y\frac{\partial C}{\partial y}\right) \\
& + \left(\frac{\partial h}{\partial y} - \sigma\frac{\partial H}{\partial y}\right)\frac{\partial}{\partial \sigma}\left\{\frac{D_y}{H}\left(\frac{\partial h}{\partial y} - \sigma\frac{\partial H}{\partial y}\right)\frac{\partial C}{\partial \sigma}\right\} + \frac{1}{H}\frac{\partial}{\partial \sigma}\left(D_z\frac{\partial C}{\partial \sigma}\right) \qquad (47)
\end{aligned}
$$

$$
\begin{aligned}
\alpha = & -\nabla\cdot\left[(\zeta+h)\left\{\left(\frac{\left(\zeta^2 - \zeta h + h^2\right)}{6} - \frac{z_\alpha^2}{2}\right)\nabla S\right.\right. \\
& \left.\left. + \left(\frac{(\zeta - h)}{2} - z_\alpha\right)\nabla T\right\}\right] \qquad (48)
\end{aligned}
$$

$$
\alpha^v = \nabla\cdot\left[\boldsymbol{\psi}\,(\zeta+h)\left\{\frac{z_\alpha^2}{2} - z_\alpha\zeta + \frac{\left(2\zeta^2 - 2\zeta h - h^2\right)}{6}\right\}\right] \qquad (49)
$$

$$
\begin{aligned}
\beta_i = & \frac{1}{2}\nabla\left({z_\alpha}^2\boldsymbol{U}_\alpha\cdot\nabla S\right) + \nabla\left(z_\alpha\boldsymbol{U}_\alpha\cdot\nabla T\right) + (T\nabla T) \\
& -\frac{1}{2}\nabla\left(\zeta^2\frac{\partial S}{\partial t^*}\right) - \nabla\left(\zeta\frac{\partial T}{\partial t^*}\right) + \left(\frac{1}{2}{z_\alpha}^2\frac{\partial \nabla S}{\partial t^*} + z_\alpha\frac{\partial \nabla T}{\partial t^*}\right) \\
& -\frac{1}{2}\nabla\left(\zeta^2\boldsymbol{U}_\alpha\cdot\nabla S\right) - \nabla\left(\zeta\boldsymbol{U}_\alpha\cdot\nabla T\right) + \nabla\left(\frac{1}{2}\zeta^2S^2\right) + \nabla(\zeta TS) \qquad (50)
\end{aligned}
$$

$$
\begin{aligned}
\beta_i^v = & \frac{(\zeta - h)}{2}\frac{\partial\boldsymbol{\psi}\zeta}{\partial t^*} - \frac{\left(\zeta^2 - \zeta h + h^2\right)}{6}\frac{\partial\boldsymbol{\psi}}{\partial t^*} + \frac{\partial}{\partial t^*}\left\{\boldsymbol{\psi}\left(\frac{z_\alpha^2}{2} - \zeta z_\alpha\right)\right\} \\
& + \frac{(\zeta - h)}{2}\nabla\left\{\boldsymbol{U}_\alpha\cdot(\boldsymbol{\psi}\zeta)\right\} - \frac{\left(\zeta^2 - \zeta h + h^2\right)}{6}\nabla\left(\boldsymbol{U}_\alpha\cdot\boldsymbol{\psi}\right) \\
& + \nabla\left[\boldsymbol{U}_\alpha\cdot\left\{\boldsymbol{\psi}\left(\frac{z_\alpha^2}{2} - \zeta z_\alpha\right)\right\}\right] \\
& - \boldsymbol{\psi}\left\{\frac{\left(\zeta^2 + \zeta h - 2h^2\right)S}{6} + \frac{(\zeta + h)\,T}{2}\right\} \qquad (51)
\end{aligned}
$$

$$
\begin{aligned}
\gamma_x = & -V_\alpha\left\{\frac{\partial z_\alpha}{\partial x^*}\left(z_\alpha\frac{\partial S}{\partial y^*} + \frac{\partial T}{\partial y^*}\right) - \frac{\partial z_\alpha}{\partial y^*}\left(z_\alpha\frac{\partial S}{\partial x^*} + \frac{\partial T}{\partial x^*}\right)\right\} \\
& - \left(\frac{\partial V_\alpha}{\partial x^*} - \frac{\partial U_\alpha}{\partial y^*}\right)\left[\left\{\frac{z_\alpha^2}{2} - \frac{\left(\zeta^2 - \zeta h + h^2\right)}{6}\right\}\frac{\partial S}{\partial y^*} + \left\{z_\alpha - \frac{(\zeta - h)}{2}\right\}\frac{\partial T}{\partial y^*}\right] \qquad (52)
\end{aligned}
$$

$$\gamma_y = U_\alpha \left\{ \frac{\partial z_\alpha}{\partial x^*} \left(z_\alpha \frac{\partial S}{\partial y^*} + \frac{\partial T}{\partial y^*} \right) - \frac{\partial z_\alpha}{\partial y^*} \left(z_\alpha \frac{\partial S}{\partial x^*} + \frac{\partial T}{\partial x^*} \right) \right\} + \left(\frac{\partial V_\alpha}{\partial x^*} - \frac{\partial U_\alpha}{\partial y^*} \right) \left[\left\{ \frac{z_\alpha^2}{2} - \frac{\left(\zeta^2 - \zeta h + h^2\right)}{6} \right\} \frac{\partial S}{\partial x^*} + \left\{ z_\alpha - \frac{(\zeta - h)}{2} \right\} \frac{\partial T}{\partial x^*} \right] \tag{53}$$

$$\gamma_y^v = -V_\alpha \left[\frac{\partial}{\partial x^*} \left\{ \psi_y \left(\frac{1}{2} z_\alpha^2 - z_\alpha \zeta \right) \right\} - \frac{\left(\zeta^2 - \zeta h + h^2\right)}{6} \frac{\partial \psi_y}{\partial x^*} + \frac{(\zeta - h)}{2} \frac{\partial \psi_y \zeta}{\partial x^*} - \frac{\partial}{\partial y^*} \left\{ \psi_x \left(\frac{1}{2} z_\alpha^2 - z_\alpha \zeta \right) \right\} + \frac{\left(\zeta^2 - \zeta h + h^2\right)}{6} \frac{\partial \psi_x}{\partial y^*} - \frac{(\zeta - h)}{2} \frac{\partial \psi_x \zeta}{\partial y^*} \right] - \left(\frac{\partial V_\alpha}{\partial x^*} - \frac{\partial U_\alpha}{\partial y^*} \right) \psi_y \left\{ \frac{z_\alpha^2}{2} - z_\alpha \zeta + \frac{\left(2\zeta^2 - 2\zeta h - h^2\right)}{6} \right\} \tag{54}$$

$$\gamma_y^v = U_\alpha \left[\frac{\partial}{\partial x^*} \left\{ \psi_y \left(\frac{1}{2} z_\alpha^2 - z_\alpha \zeta \right) \right\} - \frac{\left(\zeta^2 - \zeta h + h^2\right)}{6} \frac{\partial \psi_y}{\partial x^*} + \frac{(\zeta - h)}{2} \frac{\partial \psi_y \zeta}{\partial x^*} - \frac{\partial}{\partial y^*} \left\{ \psi_x \left(\frac{1}{2} z_\alpha^2 - z_\alpha \zeta \right) \right\} + \frac{\left(\zeta^2 - \zeta h + h^2\right)}{6} \frac{\partial \psi_x}{\partial y^*} - \frac{(\zeta - h)}{2} \frac{\partial \psi_x \zeta}{\partial y^*} \right] + \left(\frac{\partial V_\alpha}{\partial x^*} - \frac{\partial U_\alpha}{\partial y^*} \right) \psi_x \left\{ \frac{z_\alpha^2}{2} - z_\alpha \zeta + \frac{\left(2\zeta^2 - 2\zeta h - h^2\right)}{6} \right\} \tag{55}$$

in which $\nabla = (\partial/\partial x^*, \partial/\partial y^*)$, $T = (\partial h U_\alpha/\partial x^* + \partial h V_\alpha/\partial y^*)$ and $\boldsymbol{\psi} = \left(\psi_x, \psi_y\right)$. $\boldsymbol{U}_\alpha = (U_\alpha, V_\alpha)$, $\gamma_i = \left(\gamma_x, \gamma_y\right)$, and $\gamma_i^v = \left(\gamma_x^v, \gamma_y^v\right)$.

Acknowledgements The research presented in this manuscript was partially supported by grants from the Office of Naval Research (N00014-10-1-0374 and N00014-11-1- 0217) and the National Science Foundation (CMMI-06139083).

References

1. Arango HG, Moore AM, Miller AJ, Cornuelle BD, Di Lorenzo E, Neilson DJ (2004) The ROMS tangent linear and adjoint models: a comprehensive ocean prediction and analysis system. http://www.myroms.org/
2. Blumberg AF, Mellor GL (1987) A description of a three-dimensional coastal ocean circulation model. In: Heaps NS (ed) Three-dimensional coastal ocean models. American Geophysical Union, Washington, DC , pp 1–16
3. Bradford SF (2005) Godunov-based model for nonhydrostatic wave dynamics. J Waterw Port Coast Ocean Eng 131:226–238
4. Bradford SF (2011) Nonhydrostatic model for surf zone simulation. J Waterw Port Coast Ocean Eng. doi:10.1061/(ASCE)WW.1943-5460.0000079
5. Burchard H, Bolding K, Umlauf L (2012) General estuarine transport model GETM.http://www.getm.eu/
6. Chen D, Jirka GH (1995) Experimental study of plane turbulent wakes in a shallow water layer. Fluid Dyn Res 16:11–41
7. Elder JW (1959) The dispersion of marked fluid in turbulent shear flow. J Fluid Mech 5:544–560
8. Fischer HB, List EJ, Koh RCY, Imberger J, Brooks NH (1979) Mixing in inland and coastal waters. Academic press, New York
9. Haaland SE (1983) Simple and explicit formulas for the friction factor in turbulent pipe flow. J Fluid Eng 105:89–90

10. Hinterberger C, Frohlich J, Rodi W (2007) 3D and depth-averaged large-Eddy simulations of some shallow water flows. J Hydraul Eng ASCE 133(8):857–872
11. Kennedy AB, Chen Q, Kirby JT, Dalrymple RA (2000) Boussinesq modeling of wave transformation, breaking, and runup. I: 1D. J Waterw Port Coast Ocean Eng 126(1):39–47
12. Kim DH, Lynett PJ (2011) Turbulent mixing and passive scalar transport in shallow flows. Phys Fluids 23. doi:10.1063/1.3531716
13. Kim DH, Lynett PJ, Socolofsky S (2009) A depth-integrated model for weakly dispersive, turbulent, and rotational fluid flows. Ocean Model 27:198–214
14. Lacor CA, Smirnov SA, Baelmans M (2004) A finite volume formulation of compact central schemes on arbitrary structured grids. J Comput Phys 198:535–566
15. Lee SO, Kim SJ, Hwang KN, Cho YS (2009) Numerical simulations of scalar transport with full diffusion terms in the σ-coordinate system. J Coast Res 52:141–148
16. Lin P, Liu PLF (1998) Turbulence transport, vorticity dynamics, and solute mixing under plunging breaking waves in surf zone. J Geophys Res 103(c8):15677–15694
17. Lynett PJ (2006) Wave breaking effects in depth-integrated models. Coast Eng 53:325–333
18. Nadaoka K, Kondoh T (1982) Laboratory of measurements of velocity structure field in the surf zone by LDV. Coast Eng J 25:125–145
19. Nokes RI, Wood IR (1988) Vertical and lateral turbulent dispersion: some experimental results. J Fluid Mech 187:373–394
20. Phillips NA (1957) A coordinate system having some special advantages for numerical forecasting. J Meteorol 14:184–185
21. Smagorinsky J (1963) General circulation experiments with primitive equations, I. The basic experiment. Mon Weather Rev 91:99–164
22. Stansby P (1997) Semi-implicit finite volume shallow-water flow and transport solver with $k-\varepsilon$ turbulence model. Intern J Numer Methods Fluids 25:285–313
23. Stansby P, Zhou JG (1998) Shallow-water flow solver with non-hydrostatic pressure: 2D vertical plane problems. Intern J Numer Methods Fluids 28:541–563
24. Taylor GI (1953) Dispersion of soluble matter in a solvent flowing slowly through a tube. Proc R Soc Lond Ser A 219:186–203
25. Ting FCK, Kirby JT (1994) Observation of undertow and turbulence in a laboratory surf zone. Coast Eng 24:51–80
26. Toro EF (1997) Riemann solvers and numerical methods for fluid dynamics. Springer, New York
27. Toro EF (2002) Shock-capturing methods for free-surface shallow flows. Wiley, New York
28. Wang H, Dahle HK, Espedal MS, Ewing RE, Sharpley RC, Man S (1999) An ELLAM scheme for advection dispersion equations in two dimensions. SIAM J Sci Comput 20(6):2160–2194
29. Yamamoto S, Daiguji H (1993) Higher-order-accurate upwind schemes for solving the compressible Euler and Navier–Stokes equations. Comput Fluids 22(2–3):259–270
30. Yuan H, Wu CH (2004) A two-dimensional vertical non-hydrostatic sigma model with an implicit method for free-surface flows. Int Number Method Fluids 44:811—835. doi:10.1002/_d.670